MOLECULAR TOMOGRAPHIC IMAGING OF LYMPH NODES WITH NIR FLUORESCENCE[1]

Amit Joshi,[†] *Wolfgang Bangerth,*[*] *Ruchi Sharma,*[†] *John Rasmussen,*[†] *Wei Wang,*[†] *and Eva Sevick*[†]

[†]Department of Radiology, Baylor College of Medicine, Houston, TX 77030
[*]Department of Mathematics, Texas A&M University, College Station, TX 77840

ABSTRACT

This contribution describes a system and method for tomographically imaging lymph nodes marked with a lymph endothelium targeting fluorescence reporter. A novel scanning NIR laser line source was employed to acquire multiple sets of boundary fluorescence measurements in the groin region of a Yorkshire swine. The source light shaped into a linear profile was modulated at 100MHz and a gain modulated homodyne ICCD detection system was used to collect area measurements of fluorescence amplitude and phase on the illumination plane. Multiple measurement data sets generated by scanning the excitation sources were processed simultaneously to generate the interior fluorescence distribution in tissue by implementing a parallelized dual adaptive finite element based fluorescence tomography algorithm. Three dimensional localization of the approximately 2.5cm deep inguinal lymph node in the swine groin following injection of $100\mu L$ of a lymph targeting Hyaluronan-Indocyanine Green conjugate dye is demonstrated.

1. INTRODUCTION

The lymph system is thought to be responsible for the metastatic spread of cancer. Hence, the development of a molecular imaging ability for locating lymph nodes in 3-D can be a potent tool for diagnostics, image guided surgery, and monitoring response to cancer therapy. Optical agents, including fluorescent indocyanine green [1], quantum dots [2], and other organic dyes [3] have been shown to image lymph nodes in animals using planar imaging. While planar imaging is sufficient for qualitative studies, the development of a tomographic modality for locating molecular probe distribution in three dimensions is needed for quantitatively tracking probe transport through lymphatic system and for enabling accurate image guided lymph node resection procedures. As NIR light can not penetrate though the thickness of human or swine bodies, only reflectance fluorescence measurements can be acquired for locating lymph nodes.This further exacerbates the ill-posedness of the inverse problem involved in fluorescence optical tomography. In prior work, we have demonstrated localization of fluorescence targets buried in homogeneous tissue-like media from frequency domain fluorescence measurements acquired with an area illumination and area detection system. [4]. While sufficient for simple phantom experiments, a single expanded laser excitation source based measurement can not successfully reconstruct multiple fluorescence targets buried in large heterogenous volumes. We proposed and demonstrated the use of multiple spatially patterned excitation sources for tomography in resolving multiple fluorescence targets distributed in clinically relevant volumes [5]. In this contribution, we present the first practical demonstration of spatially patterned excitation based fluorescence tomography by locating the inguinal lymph node in a Yorkshire swine's groin, which was marked by a lymph endothelium specific fluorescence contrast agent synthesized in our laboratory.

[1]Part of this work has been funded through NIH grant no. R01 CA112679.

2. MATERIALS AND METHODS

2.1. Imaging subject

Yorkshire swine were chosen as imaging subjects because the swine dermis and lymphatic network is considered to be similar to human. The animal was anesthetized, intubated, and maintained with isoflurane to prevent movement. A two month old $60lb$ female swine was injected with $100\mu L$ of Hyaluronan-ICG (indocyanine green) conjugate near the mammary chains. The fluorescence activity of the injected agent was equivalent to $32\mu M$ ICG solution. The dye injection was performed while imaging with a dynamic fluorescence imaging system which showed drainage of the injected contrast agent into the lymph nodes in swine groin. Hyaluronan binds with the LYVE-1 receptor which is expressed only in lymphatic channels. After the excess agent was flushed away by the lymphatic pulsing, the vessels and the nodes were observed to be stained with the fluorescence agents and an almost steady state fluorescence signal was observed. Datasets for tomographic imaging were acquired 4 hours after the injection. The animal was euthanized after data acquisition and the lymph nodes were resected by a surgeon.

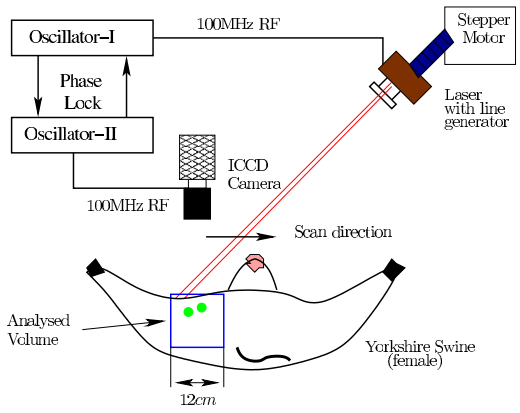

Fig. 1. Imaging system setup: NIR laser was mounted on a stepper motor to scan the line source across swine groin. Frequency domain data is acquired by using two oscillators in a homodyne mode. More details about the instrumentation are provided in Ref. [4]

2.2. Imaging system

A modified homodyne gain modulated image intensifier based CCD camera setup was used to acquire frequency domain fluorescence measurements [4]. The major components of the system are illustrated in Fig. 1. A 785 nm laser diode was mounted on a stepper motor to enable scanning across the tissue surface. The laser light was shaped into an approximately $4mm$ wide line by using a cylindrical lens. Images were acquired by an intensified CCD camera. For each laser line position on the tissue surface, frequency domain data in the form of amplitude and phase distribution on the tissue surface was acquired for excitation (785nm) and emission (830nm) wavelengths by using suitable optical filters [4]. Fig. 2 depicts sample excitation and emission images acquired by the system.

2.3. Tomography algorithm

Fluorescence optical tomography is typically performed in a model-based framework, wherein a photon transport model is used to generate predicted boundary fluorescence measurements for a given fluorescence absorption map in the tissue interior. The map of the absorption owing to fluorophore is then iteratively updated until the predicted boundary fluorescence measurements converge to the actual experimentally observed fluorescence measurements. For time dependent photon propagation in large tissue volumes, the following set of coupled photon diffusion equations adequately describes frequency domain measurements:

$$-\nabla\cdot[D_x(\mathbf{r})\nabla u(\mathbf{r})]+k_x u(\mathbf{r})=0, \quad (1)$$

$$-\nabla\cdot[D_m(\mathbf{r})\nabla v(\mathbf{r})]+k_m v(\mathbf{r})=\beta_{xm}u(\mathbf{r}). \quad (2)$$

Here,

$$D_{x,m}=\frac{1}{3(\mu_{ax,mi}+\mu_{ax,mf}+\mu'_{sx,m})},$$

$$k_{x,m}=\frac{i\omega}{c}+\mu_{ax,mi}(\mathbf{r})+\mu_{ax,mf}(\mathbf{r}), \beta_{xm}=\frac{\phi\mu_{axf}}{1-i\omega\tau(\mathbf{r})},$$

and subscripts x and m denote the excitation and the emission light fields, respectively. u, v are the complex-valued photon fluence fields at excitation and emission wavelengths, respectively; $D_{x,m}$ are the photon diffusion coefficients; $\mu_{ax,mi}$ is the absorption coefficient due to endogenous chromophores; $\mu_{ax,mf}$ is the absorption coefficient due to exogenous fluorophore; $\mu'_{sx,m}$ is the reduced scattering coefficient; ω is the modulation frequency; ϕ is the quantum efficiency of the fluorophore, and finally, τ is the fluorophore lifetime associated with first order fluorescence decay kinetics. These equations are solved with Robin-type boundary conditions on the boundary $\partial\Omega$ of the domain Ω:

$$2D_x\frac{\partial u}{\partial n}+\gamma u+S(\mathbf{r})=0, \qquad 2D_m\frac{\partial v}{\partial n}+\gamma v=0, \quad (3)$$

where n denotes the outward normal to the surface and γ is a constant depending on the optical reflective index mismatch at the boundary. The complex-valued function $S(\mathbf{r})$ is the excitation boundary source. The goal of fluorescence tomography is to reconstruct the spatial map of coefficients $\mu_{axf}(\mathbf{r})$ and/or $\tau(\mathbf{r})$ from measurements of the complex emission fluence v on the boundary. In this work we will focus on the recovery of only $\mu_{axf}(\mathbf{r})$. For notational brevity, we set $\mu_{axf}=q$ in the following paragraphs. Other optical properties were assumed to be same as that for a 1% Liposyn solution [4].

We previously proposed a novel fluorescence tomography algorithm utilizing adaptive finite element methods [6] and multiple spatially patterned excitation sources [5]. In the following, we briefly describe the formulation of the scheme and its application to lymph node image reconstructions from multiple laser line based illumination sources. M different line sources $(S^i(\mathbf{r}), i=1,2,\ldots,M)$ are employed to excite the embedded fluorophore in the phantom. Fluorescence measurements are taken on the illumination plane. The fluorescence image reconstruction problem is posed as a constrained optimization problem wherein an L_2 norm based error functional of the distance between boundary fluorescence measurements $\mathbf{z}=\{z^i, i=1,2,\ldots,M\}$ and the diffusion model predictions $\mathbf{v}=\{v^i, i=1,2,\ldots,M\}$ is minimized by variation of the parameter q, with the additional constraint that the coupled diffusion model corresponding to each illumination source $(A^i(q,[u^i,v^i])=0)$ is satisfied. In a function space setting this minimization problem reads as:

$$\min_{q,\mathbf{u},\mathbf{v}} J(q,\mathbf{v})$$

subject to

$$A^i(q;[u^i,v^i])([\zeta^i,\xi^i])=0, \qquad i=1,2,\ldots,M. \quad (4)$$

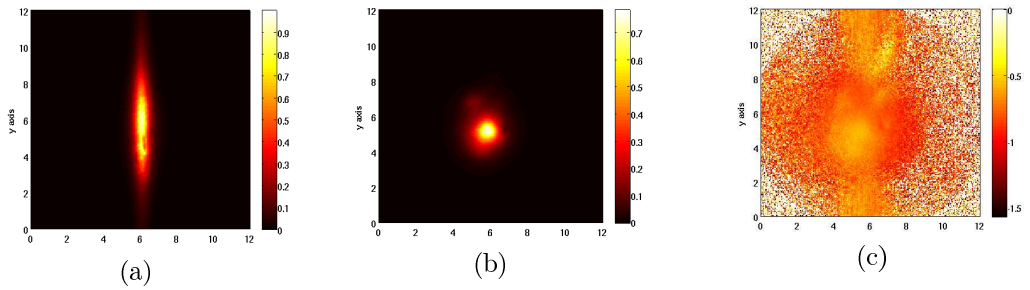

Fig. 2. Sample images acquired with the spatially patterned excitation based fluorescence imaging system: (a) Steady state excitation image (in arbitrary units), (b) Emission amplitude (a.u.), (c) Emission phase (radians). The amplitude and phase contrast created by the fluorescent lymph node is visible in the emission images.

Here, the error functional $J(q, \mathbf{v})$ incorporates a least square error term over the measurement part Γ of the boundary $\partial\Omega$ and a Tikhonov regularization term:

$$J(q, \mathbf{v}) = \sum_{i=1}^{i=m} \frac{1}{2} \left\| v^i - \sigma z^i \right\|_{\Gamma}^2 + \beta r(q). \qquad (5)$$

The parameter σ denotes the source-detector coupling coefficient which was empirically determined to be 10^{-6} in order to put the measurements and simulations on the same scale. As the image intensifier gain and the laser diode power was kept constant for all source positions, same σ was used for all i line source positions. β is the Tikhonov regularization parameter. The constraint $A^i(q; [u^i, v^i])([\zeta^i, \xi^i]) = 0$ is the weak or variational form of the coupled photon diffusion equations in frequency domain with partial current boundary conditions for the i^{th} excitation source, and with test functions $[\zeta, \xi] \in H^1(\Omega)$:

$$A^i(q; [u^i, v^i])([\zeta^i, \xi^i]) =$$
$$(D_x \nabla u^i, \nabla \zeta^i)_\Omega + (k_x u^i, \zeta^i)_\Omega + \frac{\gamma}{2}(u^i, \zeta^i)_{\partial\Omega} + \frac{1}{2}(S^i, \zeta^i)_{\partial\Omega}$$
$$+(D_m \nabla v^i, \nabla \xi^i)_\Omega + (k_m v^i, \xi^i)_\Omega + \frac{\gamma}{2}(v^i, \xi^i)_{\partial\Omega} - (\beta_{xm} u^i, \xi^i)_\Omega.$$

The solution of minimization problem (4) is determined as a stationary point of the Lagrangian [6]

$$L(x) = J(q, \mathbf{v}) + \sum_{i=1}^{i=m} A^i(q; [u^i, v^i])([\lambda_i^{ex}, \lambda_i^{em}]). \qquad (6)$$

Here, $\lambda_i^{ex}, \lambda_i^{em}$ are the Lagrange multipliers corresponding to the excitation and emission diffusion equation constraints for the i^{th} source, respectively, and we have introduced the abbreviation $x = \{\mathbf{u}, \mathbf{v}, \boldsymbol{\lambda}^{ex}, \boldsymbol{\lambda}^{em}, q\}$ for simplicity. A stationary point of $L(x)$ is found using the Gauss-Newton method wherein the update direction $\delta x_k = \{\delta \mathbf{u}_k, \delta \mathbf{v}_k, \delta \boldsymbol{\lambda}_k^{ex}, \delta \boldsymbol{\lambda}_k^{em}, \delta q_k\}$ is determined by solving the linear system

$$L_{xx}(x_k)(\delta x_k, y) = -L_x(x_k)(y) \qquad \forall y, \qquad (7)$$

where $L_{xx}(x_k)$ is the Gauss-Newton approximation to the Hessian matrix of second derivatives of L at point x_k, and y denotes the possible test functions. The Gauss-Newton equations are discretized by the finite element method. State and adjoint variables u^i, v^i, λ_i^{ex}, and λ_i^{em} for each excitation source are discretized and solved for on individual meshes with continuous finite elements, while the unknown parameter map q is discretized on a separate mesh with discontinuous finite elements. Hence for M sources, $M + 1$ finite element meshes are employed. These meshes are adaptively refined and fast Gauss-Newton updates to the unknown parameter map are calculated by carrying out the forward and adjoint computations corresponding to different sources in parallel. The mesh adaptation criteria and the parallelized Gauss-Newton update strategy is detailed in Ref. [5]. The computations were implemented with the help of open source deal.II finite element library [7].

3. RESULTS

Measurements corresponding to 6 line sources positioned symmetrically about the suspected lymph node location (as ascertained from the 2-D images) were employed. A 12cm cubical region around the suspected node location was used as the measurement and image reconstruction volume. For carrying out the finite element computation, hexahedral grids were used. Initial discretization level for all sources was kept at 1cm, while for the unknown image the initial mesh resolution was 2cm. As the Gauss-Newton parameter update iterations proceeded, the meshes for forward/adjoint computations were refined to better resolve the laser line source positions and accurately solve the photon diffusion equations, while the parameter mesh was refined to better delineate the target and coarsen the mesh in the regions away from the suspected target location. No further image update was obtained after 26 Gauss-Newton iterations during which 7 automatic mesh refinements/derefinements were triggered. Computation time was approximately 25 minutes on a 16 node Beowulf cluster

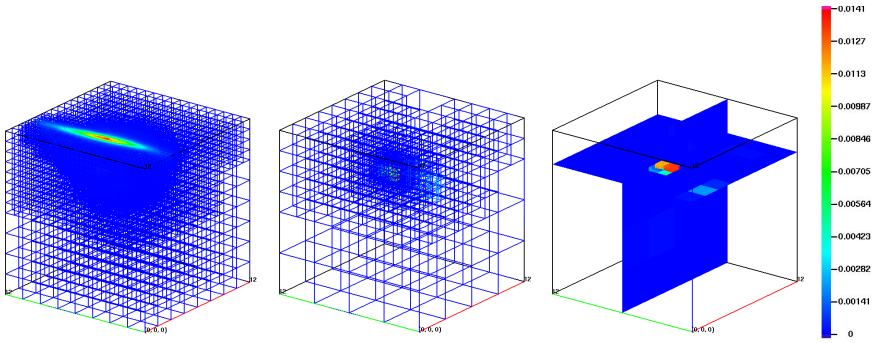

(a) (b) (c)

Fig. 3. Model based tomographic reconstruction from experimental fluorescence measurements on Swine lymph nodes: (a) Adaptively refined forward mesh depicting the first source position, (b) Final adaptively refined parameter reconstruction mesh, (c) Contour map and cutplanes drawn though the parameter reconstruction mesh depicting the reconstructed lymph node location.

with 2.2 GHz AMD opteron processors and 8 GB memory per node. 6 nodes were used for the computations reported in this paper. Fig. 3a depicts the final refined mesh for the first excitation line source. Fig. 3b,c depict the final parameter mesh and a slice plane drawn through the reconstructed μ_{axf} map. The depth of the reconstructed target was $2.5cm$ which agreed with the observation of the surgeon that the resected lymph node in the imaged location was $2.5 - 3cm$ deep.

4. CONCLUSIONS

In this preliminary study, we have demonstrated for the first time the feasibility of locating fluorescently tagged lymph nodes in intact animals from spatially patterned excitation based fluorescence optical tomography. A major weakness of this study was the use of cubical geometry for image reconstruction. The true animal surface near the animal groin had curvature which was neglected resulting in possible errors. To alleviate this concern to a degree, the legs of the animal were slightly stretched to create a nearly planar profile on the groin surface. Current work is underway on incorporating a 3D surface capturing camera system [8] with the ICCD detection setup, so that the true animal geometry can also be acquired and used for finite element simulations involved in image reconstruction. Additional improvements needed for clinical translation include the need to co-register the fluorescence images and reconstructed fluorophore maps with white light images of skin surface to ease image interpretation by non-experts, and rectifying the out of focus blur created when nonplanar surfaces are imaged by the CCD camera.

5. REFERENCES

[1] M. Gurfinek, A.B. Thompson, J. Reynolds, E. M. Sevick-Muraca, et al., "Pharmacokinetics of ICG and HPPH-car for the detection of normal and tumor tissue using fluorescence, near-infrared reflectance imaging: a case study," *Photochem. Photobiol.*, 2000.

[2] S. Kim, Y.T. Lim, E.G. Soltesz, J. Lee A. M. De Grand, A. Nakayama, J. A. Parker, T. Mihaljevic, R. G. Laurence, D. M. Dor, L. H. Cohn, M. G. Bawendi, and J.V. Frangioni, "Near-infrared fluorescent type II quantum dots for sentinel lymph node mapping," *Nature Biotechnology*, vol. 22, pp. 93–97, 2004.

[3] L. Josephson, U. Mahmood, P. Wunderbaldinger, Y. Tang, and R. Weissleder, "Pan and sentinel lymph node visualization using a near-infrared fluorescent probe," *Mol. Imaging*, 2003.

[4] A. Joshi, W. Bangerth, K. Hwang, J. Rasmussen, and E. M. Sevick-Muraca, "Fully adaptive FEM based fluorescence optical tomography from time-dependent measurements with area illumination and detection," *Med. Phys.*, vol. 33, no. 5, pp. 1299–1310, 2006.

[5] A. Joshi, W. Bangerth, and E. M. Sevick-Muraca, "Non-contact fluorescence optical tomography with scanning patterned illumination," *Optics Express*, vol. 14, no. 14, pp. 6516–6534, 2006.

[6] A. Joshi, W. Bangerth, and E. M. Sevick-Muraca, "Adaptive finite element modeling of optical fluorescence-enhanced tomography," *Optics Express*, vol. 12, no. 22, pp. 5402–5417, Nov. 2004.

[7] W. Bangerth, R. Hartmann, and G. Kanschat, `deal.II` *Differential Equations Analysis Library, Technical Reference*, 2006, `http://www.dealii.org/`.

[8] R. B. Schulz, J. Ripoll, and V. Ntziachristos, "Experimental fluorescence tomography of tissues with noncontact measurements," *IEEE Trans. Medi. Imag.*, 2004.